Dynamical Wall Following for a Wheeled Robot Using a Passive Tactile Sensor

Andrew G. Lamperski, Owen Y. Loh, Brett L. Kutscher and Noah J. Cowan

Johns Hopkins University
Baltimore, MD 21218
E-mail: {alamper1,oloh,blk1,ncowan}@jhu.edu

Abstract— **Feedback from antennae – long, flexible tactile sensors – enables cockroaches and other arthropods to rapidly maneuver through poorly lit and cluttered environments. Inspired by their performance, we created a wall-following controller for a dynamic wheeled robot using tactile antenna feedback. We show this controller is stable for a wide range of control gains and robot system parameters. To test the controller, we constructed a two-link antenna that uses potentiometers and capacitive contact sensors. Experiments based on the prototype demonstrate that our controller robustly tracks unexpected corners ranging from $-60°$ to $+90°$.**

I. INTRODUCTION

Contact and strain feedback from antennae enable cockroaches follow complex surfaces while running at speeds up to 80cm/s [1]. Inspired by this performance, we created a wall-following controller for a nonholonomic differential-drive wheeled robot that incorporates feedback from a multi-link antenna. To take full advantage of the performance envelope of the robot, we adopt a second order model that accounts for damping and inertial effects in the motors, wheels and chassis. The resulting closed-loop system is linearly stable under a wide range of control gains and system parameters. To test the controller design, we constructed a sensorized two-link antenna that measures the distance from the robot to nearby objects.

Most prior curve- and wall- following work uses sensor modalities such as vision [2]–[4] and sonar [5]–[8], since such sensors are inexpensive and widely available. However, sonar and vision exhibit sensitivity to surface reflectivity and lighting conditions. For example, sonar performance degrades in the presence of highly polished surfaces such as glass walls, and vision fails without adequate light. Infrared range-finders are also commonly used on mobile robots, but surface properties can imperil their effectiveness [9], [10]. Like ultrasonic sensors, infrared range-finders have a minimum range within which they are unreliable [10], and both sensors emit signals that betray their host's stealth.

With these limitations in mind, we suspect that well-designed "touch probes" such as antennae and whiskers will provide a compelling alternative to existing proximity sensors. Presumably, these touch probes are unaffected by surface properties such as high specularity, and environmental factors such as light and dust. In essence, most obstacles that a robot can physically hit can be sensed by touch.
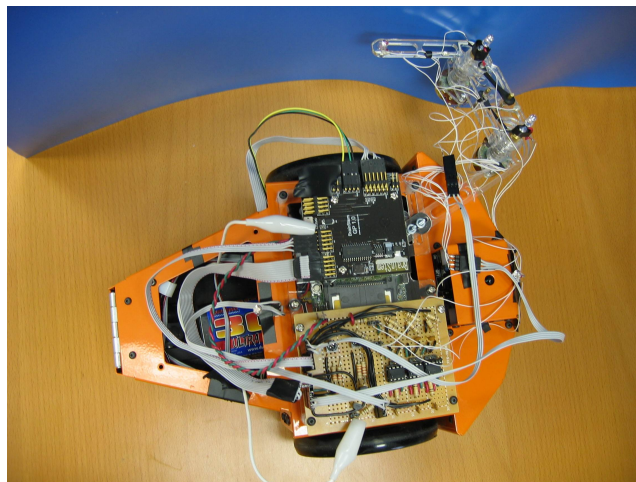

Fig. 1. The Garcia robot with a two-link sensorized antenna.

Prior work on robotic touch probes derives inspiration from two biological models: mammalian whiskers and arthropod antennae. A probe based on a mammalian whisker [11] consists of a cantilevered beam that is sensed only at its base. The base of the beam is often actuated so that the beam can be actively swept back and forth. Using this basic idea, researchers have constructed whisker-like touch sensors for object detection or recognition [9], [12], [13]. Other whisker designs are more sensitive to small features and can detect varying surface roughness [14]. Whisker-like sensors are also used as subsystems in more complicated devices such as wall-following mobile robots. Jung and Zelinsky [9] found that side-facing whiskers report distance more accurately than sonar or infrared sensors when following walls at about 3cm.

In contrast to mammalian whiskers, arthropod antennae are highly sensorized and have numerous mechanoreceptors that sense bending and contact information along the entire length of the antenna instead of solely at the base [1], [15]. Barnes, *et al.* [16] constructed a passive, large-deflection biomimetic lobster antenna equipped with three bending sensors positioned along its length. They found that their antenna can distinguish between deflections caused by object contact and fluid flow in an underwater environment. Cowan *et al.* [17] also used a high-deflection antenna for wall following in a legged robot.
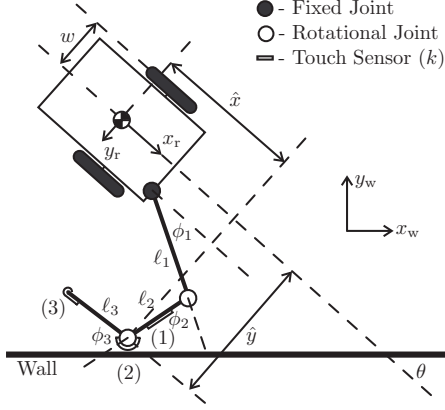
Fig. 2. *Robot schematic:* A robot, with wheel base $2w$, moves in the plane with configuration $q = (x, y, \theta, \alpha_1, \alpha_2)$, where $(x, y, \theta) \in \text{SE}(2)$ specifies the relative configuration of the robot frame axes, (x_r, y_r), to the world frame axes, (x_w, y_w), and the wheel angles (not shown) are given by $(\alpha_1, \alpha_2) \in \text{S}^1 \times \text{S}^1 = \text{T}^2$. Attached to the robot at (x_0, y_0) relative to the robot frame is an antenna that measures the look-ahead distance, $\hat{x}$, and distance-to-wall $\hat{y}$. The link angles ϕ_i denote the angle of the ith link with respect to the $(i-1)^\text{st}$ link, and each antenna link has length ℓ_i and $i = 1, 2, 3$.

This paper builds on prior work by using feedback from a single passive, sensorized antenna to enable both wall following and obstacle avoidance for a dynamic wheeled mobile robot as shown in Fig. 1. By contrast, the wall-following strategies discussed above [2], [5], [6], [9], while effective, use two "sets" of sensors – one dedicated to wall following, and one dedicated to obstacle avoidance. The single forward-facing antenna described in this paper potentially fill both roles: our wall-following controller enables wall following, while negotiating unexpected sharp bends in the wall with little additional effort.

II. MODEL AND CONTROLLER

This section describes a second order robot model and stabilizing proportional-integral (PI) control system for the robot-antenna system depicted in Fig. 2. We assume that a multi-link antenna, with negligible link inertias, provides sensor feedback from contact and angle sensors on each link as shown. In the model, each DC motor-driven wheel of the robot rolls without slipping, and we derive the equations of motion using the constraint reduction technique presented by Ostrowski [18].

A. Robot Dynamics and Reduction

The robot's position and orientation are described in SE(2) using the coordinates (x, y, θ). Additionally, the wheel positions are given by the angles (α_1, α_2). Letting m, J, and J_w be the robot mass, robot inertia, and wheel inertia respectively, the Lagrangian is written as

$$L(q, \dot{q}) = \frac{1}{2}m(\dot{x}^2 + \dot{y}^2) + \frac{1}{2}J\dot{\theta}^2 + \frac{1}{2}J_w(\dot{\alpha}_1^2 + \dot{\alpha}_2^2) \quad (1)$$

where $q = (x, y, \theta, \alpha_1, \alpha_2)$. The constraint equation,

$$A_\text{c}\dot{q} = 0, \quad (2)$$

where

$$A_\text{c} = \begin{bmatrix} \cos\theta & \sin\theta & 0 & -\frac{\rho}{2} & -\frac{\rho}{2} \\ -\sin\theta & \cos\theta & 0 & 0 & 0 \\ 0 & 0 & 1 & -\frac{\rho}{2w} & \frac{\rho}{2w} \end{bmatrix},$$

arises from the assumption that the robot's wheels roll without slipping. The parameters ρ and w denote the wheel radius and half of the wheel base, respectively (see Fig. 2).

Equivalently, (2) can be expressed as

$$\begin{bmatrix} \dot{x} \\ \dot{y} \\ \dot{\theta} \end{bmatrix} = \begin{bmatrix} \frac{\rho}{2}(\dot{\alpha}_1 + \dot{\alpha}_2)\cos\theta \\ \frac{\rho}{2}(\dot{\alpha}_1 + \dot{\alpha}_2)\sin\theta \\ \frac{\rho}{2w}(\dot{\alpha}_1 - \dot{\alpha}_2) \end{bmatrix}, \quad (3)$$

so that given the wheel velocities $(\dot{\alpha}_1, \dot{\alpha}_2)$, one can integrate (3) to obtain the pose (x, y, θ). This motivates us to "reduce" the equations of motion to be in terms of the wheel angles (α_1, α_2). Following Ostrowski [18], the reduction proceeds by writing the equations of motion as

$$\widetilde{M}\ddot{q} + A_\text{c}^T\lambda = F, \quad (4)$$

where $\lambda \in \mathbb{R}^3$ is a vector of Lagrange multipliers, $F = [0, 0, 0, \tau_1, \tau_2]^T$ denotes the torques applied to the wheels and $\widetilde{M} = \text{diag}\{m, m, J, J_w, J_w\}$ is the diagonal (non-reduced) inertia matrix.

Differentiating (2) with respect to time, substituting $\ddot{q}$ from (4), and solving for λ yields

$$\lambda = (A_\text{c}\tilde{M}^{-1}A_\text{c}^T)^{-1}(A_\text{c}\tilde{M}^{-1}F + \dot{A}_\text{c}\dot{q}). \quad (5)$$

Upon subsituting (5) and (3) into the last two rows of (4), the "reduced" dynamics can be written as

$$M\ddot{\alpha} = \tau, \quad (6)$$

where

$$M = \begin{bmatrix} J_w + \frac{m\rho^2}{4} + \frac{J\rho^2}{4w^2} & \frac{m\rho^2}{4} - \frac{J\rho^2}{4w^2} \\ \frac{m\rho^2}{4} - \frac{J\rho^2}{4w^2} & J_w + \frac{m\rho^2}{4} + \frac{J\rho^2}{4w^2} \end{bmatrix}.$$

Note that M is positive definite for all $J, J_w, m, w, \rho > 0$, which will simplify the stability analysis below.

B. Motor Dynamics and Damping Forces

A DC motor model for each wheel is given as [19]

$$V - k_\text{emf}\dot{\alpha} = L\frac{di}{dt} + Ri, \quad \tau = k_\tau i - c\dot{\alpha}, \quad (7)$$

where V and i are the input voltage and motor current respectively, and $c\dot{\alpha}$ is the frictional damping force. The motor inductance, L, armature resistance, R, torque constant k_τ, back EMF constant, k_emf and frictional damping constant c are assumed to be the same for each motor. Neglecting the term $L\frac{di}{dt}$ by assuming that the electrical dynamics are much faster the mechanical dynamics, (6) and (7) can be combined into the new system model

$$\ddot{\alpha} = A_\text{mot}\dot{\alpha} + B_\text{mot}V, \quad (8)$$

where

$$A_\text{mot} = -\left(c + k_\tau\frac{k_\text{emf}}{R}\right)M^{-1}, \quad B_\text{mot} = \frac{k_\tau}{R}M^{-1}.$$

Note that B_{mot} is invertible since it is just a scalar times M^{-1}. The inputs, V, will be functions of the antenna measurement.

C. Antenna Measurements

We assume that the joints of the multi-link antenna depicted in Fig. 2 have heavily "over-damped" springs-dampers with "fast" mechanical time constants. In other words, we assume that as the robot moves along the wall, the link angles, $\phi_i(q)$, $i = 1, 2, \ldots, n$ change as an algebraic function of the function of the robot pose. Let k denote the index of the first contact sensor touching the wall. It is straight forward to compute $(\hat{x}, \hat{y})$, the point on the antenna that is touching the wall as expressed in the current robot coordinate system:

$$\begin{bmatrix} \hat{x} \\ \hat{y} \end{bmatrix} = \begin{bmatrix} x_0 \\ y_0 \end{bmatrix} + \sum_{i=1}^{k} \ell_i \begin{bmatrix} \cos(\Psi_i) \\ -\sin(\Psi_i) \end{bmatrix} = h(\phi(q)) =: \hat{h}(q) \quad (9)$$

where $\Psi_i = \sum_{j=1}^{i} \phi_j(q)$ is the angle of the ith link with respect to the robot frame, and ℓ_i is the length of the ith link. We will refer to $\hat{x}$ as the "look-ahead distance" and $\hat{y}$ as the "distance-to-wall".

We do not need an explicit expression for the link angles, $\phi_i(q)$. The stability proofs below in Sec. II-D only require that the functions $\phi_i(q)$ (and thus also $\hat{h}(q)$) be smooth and well defined in an open neighborhood of $\theta = 0$, for a range of distances from the wall. Furthermore, our antenna design presented in Sec. III is instrumented with angular sensors at each joint to directly measure each ϕ_i.

D. Linear Controller

To define our controller, we rewrite (8) in terms of the linear and rotational velocity of the center of mass, (v, ω), since this set of coordinates proves to be intuitive and analytically simple. The velocities (v, ω) can be computed from $(\dot{\alpha}_1, \dot{\alpha}_2)$ using the similarity transform P:

$$\begin{bmatrix} v \\ \omega \end{bmatrix} = P \begin{bmatrix} \dot{\alpha}_1 \\ \dot{\alpha}_2 \end{bmatrix} = \frac{\rho}{2} \begin{bmatrix} 1 & 1 \\ -\frac{1}{w} & \frac{1}{w} \end{bmatrix} \begin{bmatrix} \dot{\alpha}_1 \\ \dot{\alpha}_2 \end{bmatrix}. \quad (10)$$

Applying P to (8) yields our state equations in terms of v and ω:

$$\begin{bmatrix} \dot{v} \\ \dot{\omega} \end{bmatrix} = A \begin{bmatrix} v \\ \omega \end{bmatrix} + B \overbrace{\begin{bmatrix} V_1 \\ V_2 \end{bmatrix}}^{u}, \quad (11)$$

where

$$A = PA_{\text{mot}}P^{-1} = \begin{bmatrix} -\frac{2(k_{\text{emf}}k_\tau + cR)}{R(2J_w + m\rho^2)} & 0 \\ 0 & -\frac{2w^2(k_{\text{emf}}k_\tau + cR)}{R(J\rho^2 + 2J_w w^2)} \end{bmatrix},$$

$$B = PB_{\text{mot}} = \begin{bmatrix} \frac{k_\tau \rho}{2J_w R + m\rho^2 R} & \frac{k_\tau \rho}{2J_w R + m\rho^2 R} \\ -\frac{k_\tau \rho w}{J\rho^2 R + 2J_w R w^2} & \frac{k_\tau \rho w}{J\rho^2 R + 2J_w R w^2} \end{bmatrix}.$$

Note that B is invertible, since P and B_{mot} are both invertible.

The system (11) can be controlled with a PI controller:

$$\begin{bmatrix} u_1 \\ u_2 \end{bmatrix} = \begin{bmatrix} -k_1(v - v^*) - k_2\Sigma \\ k_3(\hat{y} - d^*) - k_4\omega \end{bmatrix}, \ \Sigma = \int_0^t (v - v^*)dt, \quad (12)$$

where v^* is the desired forward speed and d^* is the desired distance to the wall. To map the torques into motor voltages, the control law (12) becomes $V = B^{-1}u$.

Combining the kinematics (3), the change of coordinates (10), the system dynamics (11), and the control law (12), yields the complete nonlinear system equation as expressed in the world coordinate system

$$\begin{bmatrix} \dot{y} \\ \dot{\theta} \\ \dot{\Sigma} \\ \dot{v} \\ \dot{\omega} \end{bmatrix} = \begin{bmatrix} v \sin\theta \\ \omega \\ v - v^* \\ A \begin{bmatrix} v \\ \omega \end{bmatrix} + \begin{bmatrix} -k_1(v - v^*) - k_2\Sigma \\ k_3(\hat{y} - d^*) - k_4\omega \end{bmatrix} \end{bmatrix}, \quad (13)$$

where x has been removed for simplicity since it does not affect any of the other states. Equipped with the full state equation, it is now possible to analyze the stability of the proposed control law by linearizing the system and looking at the roots of the characteristic polynomial. To do so, note that $\hat{y}$ can be removed from the control law (12) by noting that $\hat{y} = -\frac{y}{\cos\theta} - \hat{x}(q)\tan\theta$, where $\hat{x}(q)$ is found using $\hat{h}(q)$ in (9). Linearizing (13) around

$$[y, \theta, \Sigma, v, \omega]^T = [-d^*, 0, ([A]_{1,1}/k_2)v^*, v^*, 0]^T \quad (14)$$

and taking Hurwitz determinants of of the characteristic polynomial reveals sufficient conditions for asymptotic stability:

$$a, b, k_2, k_3, v^*, \hat{x}^* > 0, \quad b\hat{x}^* > v^*, \quad 2k_2 > k_3,$$
$$a^2\hat{x}^* + ab\hat{x}^* + k_3\hat{x}^{*2} > 2bv^* + 3av^* + 2k_2\hat{x}^*. \quad (15)$$

The condition $\hat{x}^* > 0$ is satisfied by assuming that the antenna is designed to have a positive look-ahead distance when $\theta = 0$. The remaining constraints can be satisfied by a number of gain combinations, e.g.: $a = 10$, $b = 4$, $k_2 = 8$, $k_3 = 10$, $v^* = 0.30$, $\hat{x}^* = 0.10$.

An interesting observation about the conditions for stability is that they don't depend on $\hat{x}(q)$ or its partials, as these terms disappear during the linearization (specifically, they get multiplied by $\sin\theta_0$ or $\tan\theta_0$ where $\theta_0 = 0$). This observation leads to an important result for antenna based navigation: the system is not affected by the antenna configuration.

E. Switching Control Scheme

Though the linearized controller is stable near the system's equilibrium position, it fails to account for two important cases when the robot is far from its equilibrium and the antenna behaves poorly. Each of these cases is handled by a separate heuristic algorithm as described below. In the cases when these algorithms are applied, the local stability proof in section II-D is no longer valid, though the system seems stable in practice.

a) Regaining wall contact: If the robot loses contact with the wall, the control scheme switches to an open loop strategy that steers the robot in a smooth arc back towards the wall. We have found anecdotally that steering the robot "just past" where contact was lost often returns the robot back within the basin of attraction of our controller

(12). A limited near-field range of operation is an inherent limitation of tactile sensors, and in the future we intend to treat this situation more carefully.

b) Recovering from corners: When the robot encounters a corner, the second rotational joint of the antenna buries itself into the corner, causing the antenna to report a constant distance to the wall. In response to this data, the robot continues to run straight until the first rotational joint touches the wall, causing k in (9) to change from 2 to 1. At this point, the robot is too close to the corner to follow it using (12), so the controller applies a sharp torque to the robot that steers it out of the corner and avoids a collision. This situation does *not* seem to be an inherent limitation of antenna sensors and we suspect that improved antenna designs will mitigate this problem. At that point, this heuristic will be unnecessary.

F. System Identification

Since not all of the parameters are supplied by the robot manufacturer used in the experiments (Sec. V), we performed system identification. To accomplish this, we supplied the robot with known voltage commands, and stored wheel velocities at a sampling interval Δt. Due to the structure of $A = \text{diag}\{a_1, a_2\}$ and B, the dynamical equation (11) for (v, ω) can be rewritten as

$$\begin{bmatrix} \dot{v} \\ \dot{\omega} \end{bmatrix} = \begin{bmatrix} a_1 v \\ a_2 \omega \end{bmatrix} + \begin{bmatrix} (V_1 + V_2)b_1 \\ (-V_1 + V_2)b_2 \end{bmatrix}, \qquad (16)$$

where $V \in \mathbb{R}^2$ corresponds to input voltage, and (a_1, a_2, b_1, b_2) are the four unknown parameters to be fit.

Since we have sampled data, we fit a discrete time model based on the the structure of (16). The discrete time matrices are

$$A_d = e^{A \Delta t}, \quad B_d = \left(\int_0^{\Delta t} e^{A(\Delta t - \sigma)} d\sigma \right) B. \qquad (17)$$

The simple structure of A and B ensure that the discrete matrices have the same structures as their continuous counterparts. Thus, letting $x^j = \begin{bmatrix} v(t_j) & \omega(t_j) \end{bmatrix}^T$ denote the state at time t_j, we can form a least squares fitting equation of the form

$$\begin{bmatrix} x^2 \\ \vdots \\ x^{p+1} \end{bmatrix} = \begin{bmatrix} x_1^1 & 0 & V_1^1 + V_2^1 & 0 \\ 0 & x_2^1 & 0 & -V_1^1 + V_2^1 \\ & & \vdots & \\ x_1^p & 0 & V_1^p + V_2^p & 0 \\ 0 & x_2^p & 0 & -V_1^p + V_2^p \end{bmatrix} \begin{bmatrix} a_1^d \\ a_2^d \\ b_1^d \\ b_2^d \end{bmatrix}$$

(18)

where $a_1^d, a_2^d, b_1^d, b_2^d$ are the discrete time entries of the matrices A_d and B_d. Using the least-squares solution to (18) provides the discrete time matrices A_d and B_d. To get the continuous model, we see from (17),

$$A = \frac{1}{\Delta t} \log A_d, \quad B = \left(e^{A \Delta t} \int_0^{\Delta t} e^{-A \sigma} d\sigma \right)^{-1} B_d.$$

With these estimates and the direct measurements of ρ and w of the robot, we can implement the controller.
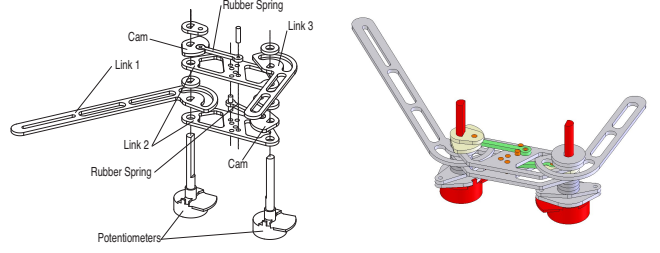

Fig. 3. **Left:** The antenna is assembled by sliding the links onto the potentiometer shafts (some spacers and other minor parts are omitted from this figure for simplicity). The base of each potentiometer is fixed to the center link. **Right:** Fully assembled model.

III. ANTENNA DESIGN AND CONSTRUCTION

We constructed a two-link passive tactile antenna with three rigid polycarbonate segments hinged on commercial potentiometers (see Fig. 3). The electrical resistance of each potentiometer determines ϕ_i, the angle of the link i with respect to link $i - 1$ (see Fig. 2). These angles determine the distance and orientation of the body with respect to the wall as described in Sec. II. A rubber spring-cam mechanism acts as a torsion spring on each joint. The inherent friction in the potentiometers serves to damp the system. Touch sensors are integrated along the leading edge of each link to determine the region of contact.

Each structural segment of the antenna consists of a rigid linkage and a potentiometer. (see Fig. 3) The rigid links are laser cut from 1/8" clear polycarbonate sheet. The first segment is fixed rigidly to the robot and is considered an extension of the body. The base of each of the two potentiometers is fixed to the center link while the shaft of each is fixed to the end of the adjacent link. This gives each joint one degree of freedom with respect to the adjacent links. Though this particular antenna uses two links, the modular design enables the addition of more links.

A. Spring-Cam Design: Locally Linear Spring

The rubber spring-cam torsion springs constrain the motion of each link about a preset nominal angle. For small displacements, the torque applied by the spring is linear, as shown below. For a given displacement θ, the length of the spring is defined as

$$\ell = \sqrt{\ell_0^2 + 2r_c^2 - 2r_c(r_c + \ell_0) \cos \theta + 2r_c \ell_0}. \qquad (19)$$

The potential energy stored in the spring is $E(\theta) = \frac{1}{2}\kappa(\ell - \gamma)^2$, where κ is the spring constant of the rubber and γ is the unstrained length of the spring. Taking the derivative of the potential energy yields the torque, τ, applied by the spring about the axis of the joint:

$$\tau = \frac{\kappa r_c(r_c + \ell_0)(\ell - \gamma)}{\ell} \sin \theta. \qquad (20)$$

This expression for τ is locally linear about $\theta = 0$ so long as the spring is given a preset tension, i.e. $\gamma < \ell_0$.

Stiffness of the springs is varied either through the preset tension or the hardness of the rubber used. Based on the results of simulations run (see Sec. IV), the links are given

progressively lower stiffness. Since the mass of each link is dominated by the potentiometers, no effort is made to optimize mass distribution.

B. Sensor Integration

Each joint is based on a 2 kΩ linear taper carbon volume control potentiometer by Calrad Electronics. The potentiometers are calibrated such that the measured resistance corresponds linearly to a known angle. Based on angle-voltage data, the linearity of the angle-resistance relation has a correlation coefficient of better than 90%.

Capacitive touch sensors (QProx Research QT111D Charge-Transfer Touch Sensors) are attached to each link, on the leading edge of the joint. This enables the sensor to determine which region of the antenna is in contact with the wall. For each sensor, the integrated circuit and all required circuitry are carried on board the robot while a single wire lead is run to the antenna. To increase the sensitive area, the leading edge of each link is coated with a conductive epoxy. The same epoxy is used to fix the lead wire to the conductive area.

IV. SIMULATIONS

To explore the antenna design space and controller performance, we performed numerical simulations with Matlab, using the full dynamical model of Sec. II. In addition, we model the antenna as a fully dynamic, planar n-link kinematic chain, coupled to the robot. To capture dynamic effects, each link is represented by a point mass, m_i, and each joint has a torsional spring, k_i, and damper, b_i.

A. Simulated Dynamics

We simulated the Euler-Lagrange equations for the robot with dynamic antenna, based on the Lagrangian $L = T - V$, computed as follows. In terms of the configuration, $q_e = (x, y, \theta, \alpha_1, \alpha_2, \phi_1, \ldots, \phi_n)$, the kinetic energy is given by

$$T = \frac{m}{2}(\dot{x}^2 + \dot{y}^2) + \frac{J}{2}\dot{\theta}^2 + \frac{J_w}{2}(\dot{\alpha}_1^2 + \dot{\alpha}_2^2) + \sum_{i=1}^{n} \frac{m_i}{2} \|\nu_i\|^2,$$

where ν_i denotes the velocity of the ith link mass (readily computed from $q_e, \dot{q}_e$). The potential energy stored in the joint springs and is given by

$$V = -\sum_{i=1}^{n} k_i \cos(\phi_i - \phi_i^*), \qquad (21)$$

where ϕ_i^* is the ith equilibrium angle. Note: V is in terms of cosine potentials because they are continuous on S^1.

Using the Lagrangian above, and the kinematic nonholonomic constraints from (2), we implemented a Matlab simulation of the controlled robot subject to (12). Several additional forces were included in the simulation. The walls, modeled as one-sided spring-dampers, exert normal forces on every link. To ensure realistic simulations, the wall spring/damper constants are at least two orders of magnitude greater than those of the antenna joints. Sliding friction between the antenna and wall was neglected.

B. Determining good initial antenna configurations

For simulation purposes, we determined reasonable initial antenna configurations as follows. For a given robot configuration (x, y, θ), we found the antenna configuration, $\phi_1 \ldots, \phi_n$, that gives the minimum potential energy (21), subject to the inequality constraint that the antenna cannot pass through the wall. Since there are n links, and each one either touches or does not touch the wall, there are 2^n possible contact configurations. If $S = \{1, \ldots, 2^n\}$, then for each subset $s \subset S$, $|s| = p$, we have p constraint equations $g_{s_1}(q) = \cdots = g_{s_p}(q) = 0$, each corresponding to link s_i making contact with the wall. To minimize $V(q)$ subject to the constraints, we found the condition when $\nabla V = \sum_{i=1}^{p} \mu_i \nabla g_i$, where μ_i are Lagrange multipliers.

C. Simulation Results

We designed our simulations so that we could readily change parameters such as the number of links, spring and damping constants, link masses and equilibrium configuration. By examining how behavior changed with variation of parameters, we formed hypotheses of which properties might be important in the design of a real antenna. While looking at robot behavior in negative angle turns (as in the figure), we saw the need for contact sensors to detect which link was touching the wall. These contact sensors proved vital in detecting loss of contact with the wall and collision avoidance. Furthermore, our simulations showed that the first link must be short enough such that, when it is touching the wall, $\hat{y}$ never exceeds d^*, the desired displacement from the wall.

Simulations of antenna relaxation indicated that settling times improved by progressively decreasing mass and stiffness along the length of the antenna. Intuitively, decreasing mass and stiffness decreases the forces produced at large displacements from the base, thus decreasing the moments induced on the antenna. In experiments, the antenna appeared to settle on a faster time scale than the robot dynamics. Thus we did not attempt to optimize mass distribution of the antenna.

V. EXPERIMENTS

For the experiments, the control law (12) ran at 50Hz on an ARM processor embedded in a commercially available wheeled robot (Garcia from Acroname). An overhead camera tracked two LED's on Garcia to obtain the ground truth position of the robot. For each of the trials, Garcia ran autonomously at 10cm/s along walls with corners ranging from $-90°$ (a concave right angle corner) to $+90°$ (a convex right angle corner). The results for a run with a $-30°$ corner are shown in Fig. 4.

Table I summarizes the results of all of the experiments. Garcia successfully followed walls that contained angles between $+90°$ and $-60°$. Rise time was computed as the time taken to rise from 10% to 90% of the final value. The $-90°$ runs failed because the first (most proximal) link of the antenna hit the wall before the second or third link, and the first link was rigidly attached to the robot causing a

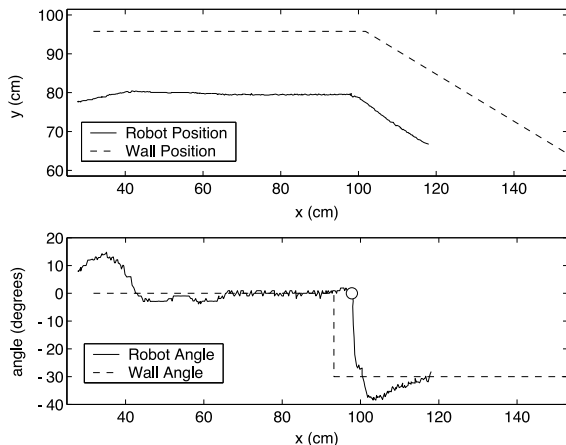| Wall Angle (deg)	# Trials	% Success	Rise Time(s)
+90	10	100%	(unavailable)
+60	10	100%	3.0±0.11
+30	10	100%	2.4±0.2
-30	10	100%	0.52±0.18
-60	10	100%	0.64±0.06
-90	5	0%	(unavailable)

TABLE I

SUMMARY OF EXPERIMENTS.

Fig. 4. *Experimental Run:* **Top:** The path traversed by the robot while running along a −30° wall. **Bottom:** The angle of the robot during that same trial. Note: the angle step occurs when the antenna first touches the corner. At 96cm (denoted ○) contact sensor 1 touches the wall (Sec. II-E).

hard collision. A more flexible antenna design should help mitigate this problem. The negative angles (concave walls) had faster performance because of the high controller gains used whenever the more proximal links contacted the wall.

VI. DISCUSSION

Several problems arose during experimental testing due to the fact that we used a rigid, low dimensional engineering model for our antenna. Improving the design of this antenna represents work-in-progress, and while the simulations in Sec. IV provide useful hints that may help, we seek more fundamental design principles for "good" antenna size, shape and stiffness.

Next, we wish to equip hexapedal robots such as RHex [20] and Sprawl [21] with antennae, by incorporating "multi-stride" dynamics [22] into the controller design. The integration of a high performance bio-inspired robot with a dynamic bio-inspired sensor will provide new opportunities to compare the performance of man-made robots with natural creatures like the cockroach.

ACKNOWLEDGMENTS

REFERENCES

[1] J. M. Camhi and E. N. Johnson, "High-frequency steering maneuvers mediated by tactile cues: antenna wall-following in the cockroach," *J Exp Bio*, vol. 202, pp. 631–643, 1999.

[2] A. K. Das, R. Fierro, V. Kumar, B. Southall, J. Spletzer, and C. Taylor, "Real-time vision-based control of a nonholonomic mobile robot," in *International Conference on Robotics and Automation*, 2001, pp. 1714–1719.

[3] Y. Ma, J. Košecká, and S. S. Sastry, "Vision guided navigation for a nonholonomic mobile robot," *IEEE Transactions on Robotics and Automation*, vol. 15, no. 3, pp. 521–536, June 1999.

[4] S. Skaff, G. Kantor, D. Maiwand, and A. A. Rizzi, "Inertial navigation and visual line following for a dynamical hexapod robot," in *Intelligent Robots and Systems*. Las Vegas, NV: IEEE, 2003.

[5] A. Bemporad, M. Di Marco, and A. Tesi, "Sonar-based wall-following control of mobile robots," *Journal of Dynamic Systems, Measurement, and Control*, vol. 122, no. 1, pp. 227–230, March 2000.

[6] R. Carelli and E. O. Freire, "Corridor navigation and wall-following stable control for sonar-based mobile robots," *Robotics and Autonomous Systems*, vol. 45, pp. 235–247, 2003.

[7] T. Yata, L. Kleeman, and S. Yuta, "Wall following using angle information measured by a single ultrasonic transducer," in *IEEE International Conference on Robotics and Automation*, 1998, pp. 1590–1596.

[8] H. Noborio, I. Yamamoto, and T. Komaki, "Sensor-based path-planning algorithms for a nonholonomic mobile robot," in *International Conference on Intelligent Robots and Systems*, 2000, pp. 917–924.

[9] D. Jung and A. Zelinsky, "Whisker-based mobile robot navigation," in *Proceedings of the IEEE/RSJ International Conference on Intelligent Robots and Systems (IROS)*, vol. 2, November 1996, p. 497.

[10] C. R. Kube, "A minimal infrared obstacle detection scheme," *The robotics Practitioner: The Journal for Robot Builders*, vol. 2, no. 2, pp. 15–20, 1996.

[11] M. J. Hartmann, N. J. Johnson, R. B. Towal, and C. Assad, "Mechanical characteristics of rat vibrissae: Resonant frequencies and damping in isolated whiskers and in teh awake behaving animal," *Journal of Neuroscience*, vol. 23, no. 16, pp. 6510–6519, 2003.

[12] R. A. Russell, "Object recognition using articulated whisker probes," in *Intl. Symp. of Intelligent Robotics*, Tokyo, 1985, pp. 605–11.

[13] M. Kaneko, N. Kanayama, and T. Tsuji, "Active antenna for contact sensing," in *IEEE Transactions on Robotics and Automation*, ser. 2, vol. 14, April 1998.

[14] M. Lungarella, V. V. Hafner, R. Pfeifer, and H. Yokoi, "An artificial whisker sensor for robotics," in *Proceedings of the 15th IEEE/RSJ International Conference on Intelligent Robots and Systems (IROS)*, Lausanne, Switzerland, 2002, pp. 2931–2936.

[15] J. Okada and Y. Toh, "The role of antennal hair plates in object-guided tactile orientation of the cockroach (periplaneta americana)," *Journal of Comparative Physiology A-Neuroethology Sensory Neural and Behavioral Physiology*, vol. 186, no. 9, pp. 849–857, 2000.

[16] T. Barnes, T. Truong, G. Adams, and N. McGruer, "Large deflection analysis of a biomimetic lobster robot antenna due to contact and flow," *Transactions of the ASME*, vol. 68, pp. 948–951, 2001.

[17] N. J. Cowan, E. J. Ma, M. Cutkosky, and R. J. Full, "A biologically inspired passive antenna for steering control of a running robot," in *International Symposium on Robotics Research*, Siena, Italy, 2003.

[18] J. Ostrowski, "Computing reduced equations for robotic systems with constraints and symmetries," *IEEE Transactions on Robotics and Automation*, 1998.

[19] D. G. Alciatore and M. B. Histand, *Introduction to mechatronics and measurement systems*, 2nd ed. McGraw-Hill, 2003.

[20] U. Saranli, M. Buehler, and D. E. Koditschek, "RHex: A simple and highly mobile hexapod robot," *The Internatiional Journal of Robotics Research*, vol. 20, no. 7, pp. 616–631, 2001.

[21] J. G. Cham, S. A. Bailey, J. E. Clark, R. J. Full, and M. R. Cutkosky, "Fast and robust: Hexapedal robots via shape deposition manufacturing," *The International Journal of Robotics Research*, vol. 21, no. 10, 2002.

[22] A. J. McClung, J. G. Cham, and M. R. Cutkosky, "Rapid maneuvering of a biologically inspired hexapedal robot," in *International Mechanical Engineering Congress*. Anaheim, California: ASME, Nov 2004.